Corrosion Science 177 (2020) 108956

Contents lists available at ScienceDirect

Corrosion Science

journal homepage: www.elsevier.com/locate/corsci

# Oxidation behaviour of NiAl intermetallics with embedded Cr and Mo

Golnar Geramifard [a,*], Camelia Gombola [b], Peter Franke [a], Hans J. Seifert [a]

[a] Karlsruhe Institute of Technology, Institute for Applied Materials (IAM-AWP), Eggenstein-Leopoldshafen, 76344, Germany
[b] Karlsruhe Institute of Technology, Institute for Applied Materials (IAM-WK), Karlsruhe, 76131, Germany

ARTICLE INFO

*Keywords:*
NiAl-Cr
NiAl-Mo
Directional solidification
Oxidation
Diffusion
CALPHAD

ABSTRACT

The isothermal oxidation of directionally solidified NiAl-34Cr and NiAl alloys with embedded Cr bar and Mo wire were studied in a thermobalance at 800 °C, 1200 °C and 1300 °C for 50 h (Ar/ 13 vol.% $O_2$). NiAl-Cr showed formation of a continuous $Al_2O_3$-$Cr_2O_3$ solid solution in the vicinity of the interface of NiAl and Cr in which the composition changed from almost pure $Al_2O_3$ near the metal matrix to almost pure $Cr_2O_3$ near the gas surface. DS NiAl-34Cr showed more spallation compared to NiAl-Cr. In case of NiAl-Mo, a weight loss was observed due to formation of volatile oxides.

## 1. Introduction

In the past few decades, gas turbine manufacturers used Ni-based superalloys to increase the tolerated gas inlet temperature in the combustion chamber and, consequently, to increase the operational efficiency. However, the operating temperatures in the engines are currently near the solidus temperatures of the materials used. Therefore, there is a need for alternative alloys which can withstand higher temperatures. NiAl-based intermetallics are proposed and have been investigated in recent decades with promising results [1]. However, unsuitable mechanical properties of pure NiAl, such as poor ductility and fracture toughness at room temperature along with an insufficient creep resistance and low strength at high temperatures, require improvements in the manufactured alloys [2].

The NiAl has a higher melting temperature than the solidus temperature of Ni-based superalloys. In addition, directionally solidified metal-matrix composites of NiAl alloy, in which fibres of chromium or molybdenum are embedded, show much better mechanical properties than pure NiAl [3–9]. This makes these composites candidates for high-temperature applications in turbines since they also exhibit good thermodynamic stability and chemical compatibility between the NiAl matrix and the strengthening fibres.

However, the metal matrix composites will be in contact with oxygen-containing combustion gases in the turbine and oxidative corrosion processes are inevitable. During oxidation of NiAl, the formation of γ-$Al_2O_3$, θ-$Al_2O_3$ and σ-$Al_2O_3$ as metastable phases are reported [10–12] which are transformed into stable α-$Al_2O_3$ after further heating [13,14].

The oxidation behaviour of both NiAl-Cr and NiAl-Mo composites is of interest due to the fact that, in addition to α-$Al_2O_3$, which is formed during oxidation of NiAl at high temperatures, $Cr_2O_3$ and various volatile Mo oxides can form, respectively [15]. Compared to the number of studies on mechanical properties, there are much fewer reports on oxidation behaviour of directionally solidified NiAl-based eutectic alloys [15,16].

In the present work, oxidation processes are investigated by advanced computational and experimental thermodynamics in the material systems NiAl-Cr-O and NiAl-Mo-O. The investigations are focused on Ni-Al-Cr-Mo alloys with equimolar ratio of Ni:Al.

The present authors have compiled a thermodynamic database for Ni, Al, Cr, Mo and O [17], which includes assessed binary and ternary systems. Different oxides which can form during oxidation of NiAl-Cr and NiAl-Mo are included in the database, e.g. α-$Al_2O_3$, $Cr_2O_3$, NiO, as well as the spinel phases and metastable oxides, which can form at lower temperatures or in the initial stages of oxidation. This database was used for thermodynamic calculations using the Thermo-Calc software [18] to determine the phase diagrams (including isoplethic and isothermal sections) and heterogeneous phase reactions and to predict suitable operating ranges (temperatures and oxygen activities) for metal matrix composites in turbine applications.

In order to investigate the oxidation behaviour of NiAl-Cr and NiAl-Mo interfaces, coarse composites were produced by embedding Cr pieces and Mo wires into a NiAl matrix by using an arc-melter. These samples are named coarse composites of NiAl-Cr and NiAl-Mo in order to

* Corresponding author.
*E-mail address:* golnar.geramifard@kit.edu (G. Geramifard).

https://doi.org/10.1016/j.corsci.2020.108956
Received 23 April 2020; Received in revised form 24 July 2020; Accepted 17 August 2020
Available online 21 August 2020

distinguish them from the directionally solidified samples (DS). The samples were oxidized under an Ar atmosphere containing 13 vol.% $O_2$ in a thermobalance. Subsequently, the compositions and the microstructures of the oxidation products at the surface and the interface of NiAl and the embedded phase of Cr or Mo were investigated by X-ray diffraction (XRD), scanning electron microscopy (SEM) equipped with energy dispersive X-ray analysis (EDX), electron backscatter diffraction (EBSD) and electron probe micro-analyzer (EPMA).

DS NiAl-34Cr samples were produced using zone melting with induction heating and were oxidized under similar conditions. The results are discussed and compared with the coarse composite of NiAl-Cr.

## 2. Experimental methods

### 2.1. Sample preparation

NiAl with equimolar Ni:Al compositions were prepared from high-purity aluminium shot (99.99 wt.%) and nickel shot (99.95 wt.%) using an electric arc furnace (AM0.5, Edmund Bühler) under an argon atmosphere (99.9999 % purity). To ensure compositional homogeneity, each alloy button was turned over and re-melted at least five times. Nominal compositions were accepted since the weight loss after melting did not exceed 0.1 mass %.

Coarse composites of NiAl-Cr and NiAl-Mo were produced by placing chromium bars or molybdenum wires in the cylindrical mold of an arc-melting device and then casting molten NiAl over them. The resulting rods of NiAl with embedded Cr or Mo were cut with a diamond saw to samples of approximately 10 mm in diameter and between 1.5–3 mm in thickness as shown in Fig. 1-a and b. In Fig. 1-a, the NiAl-Cr coarse composite is shown. Although a good contact between the Cr (the brighter region of the sample) and NiAl (the darker region of the sample) was made, pores could not be avoided completely at the interface of NiAl and the chromium bar. The Fig. 1-b shows the NiAl-Mo coarse composite where the brighter region of the sample is the molybdenum wire and the darker region is the solidified NiAl which was cast over the molybdenum wire. Samples of pure NiAl without any embedded materials were also produced to validate the oxidation results in this work by comparing them with the work by Brumm and Grabke [19] who investigated the oxidation of pure NiAl. In addition, directionally solidified samples of NiAl with 34 at.% Cr were prepared. For this purpose, buttons were first produced, which were then melted again and cast into a cylindrical copper mold with a diameter of 12.5 mm and a length of 180 mm. Finally, the rods were directionally solidified by zone melting with an induction coil similar to the method of Johnson et al. [8] with a growth rate of 120 mm $h^{-1}$.

Before oxidation, all specimens were ground with SiC abrasive to a maximum of 1200 grit. Then they were cleaned in an ultrasonic bath using iso-propanol for 10 min.

For surface investigations by SEM the samples were coated with graphite. For cross section investigations by SEM and EBSD, specimens were completely embedded in resin or graphite epoxy, respectively. Then they were abraded at the desired surface to reveal the interface of NiAl and Cr and further ground to a maximum of 1200 grit and polished down to 1 μm surface finish.

Some samples were also etched with a solution of 80 vol.% $H_2O$, 10 vol.% HCl (37 % w/w) and 10 vol.% $H_2O_2$ (30 % w/w) to better reveal the microstructure.

### 2.2. Oxidation procedure

The samples were investigated by thermogravimetric analysis (TGA) (Netzsch STA 449) for 50 h at temperatures of 800 °C, 1200 °C and 1300 °C under oxidizing condition with the total flow of 10 L· $h^{-1}$ (Ar/13 vol.% $O_2$). The heating rate to reach the desired temperatures was 20 °C ·$min^{-1}$. The specimens were placed on top of $Al_2O_3$ or $ZrO_2$-crowns in the TGA in order not to block the oxygen flow on one side of the sample. The mass change during oxidation was recorded by the microbalance. After oxidation, the oxide layers were investigated both on the surface and in cross sections, using XRD, SEM, EDX, EPMA and EBSD.

## 3. Results and discussion

### 3.1. Oxidation of NiAl, NiAl-Cr coarse composite and DS NiAl-34Cr

When pure metals are oxidized, the growth of the oxide layer is governed by the parabolic law [20]. However, in higher order systems the parabolic law is not strictly valid due to the fact that the activities at the phase boundaries are no longer fixed. Nevertheless, an approximate parabolic behaviour often found experimentally in higher order systems [20–22].

In this work, the mass gains of NiAl, NiAl-Cr coarse composite and DS NiAl-34Cr samples were recorded continuously in the TGA. As can be seen in Fig. 2-a, oxidation rates increased with increasing temperature. At a temperature of 800 °C, the mass gain of NiAl and the coarse composite of NiAl-Cr (curves 8 and 5, overlapping) show parabolic behaviour which indicates that the kinetics of oxide growth is diffusion controlled [20–22].

At 1200 °C, the DS NiAl-34Cr (curve 2) sample has the highest oxidation rate compared to NiAl-Cr (curve 4) and NiAl (curve 7). The spallation of oxide scales has already started as can be seen in the fluctuation of the mass gain (shown with arrows at curve 2) at this

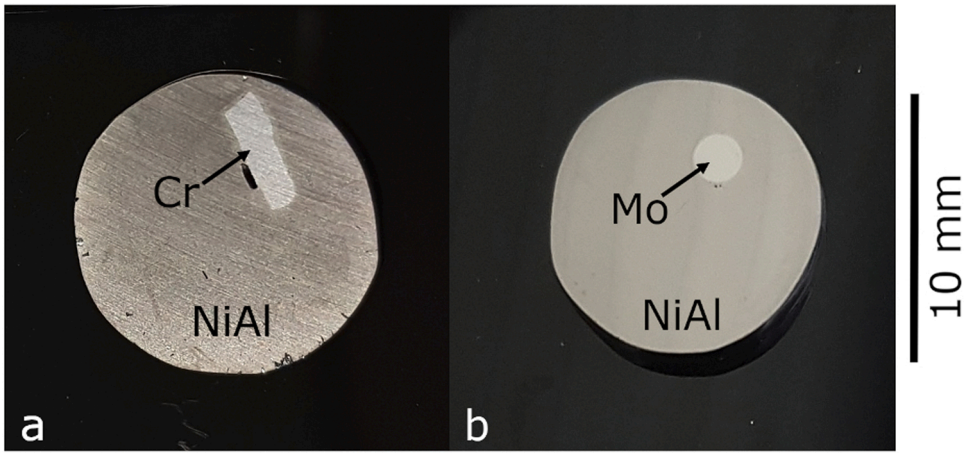


**Fig. 1.** NiAl with embedded Cr and Mo. a) NiAl-Cr coarse composite, b) NiAl-Mo coarse composite.

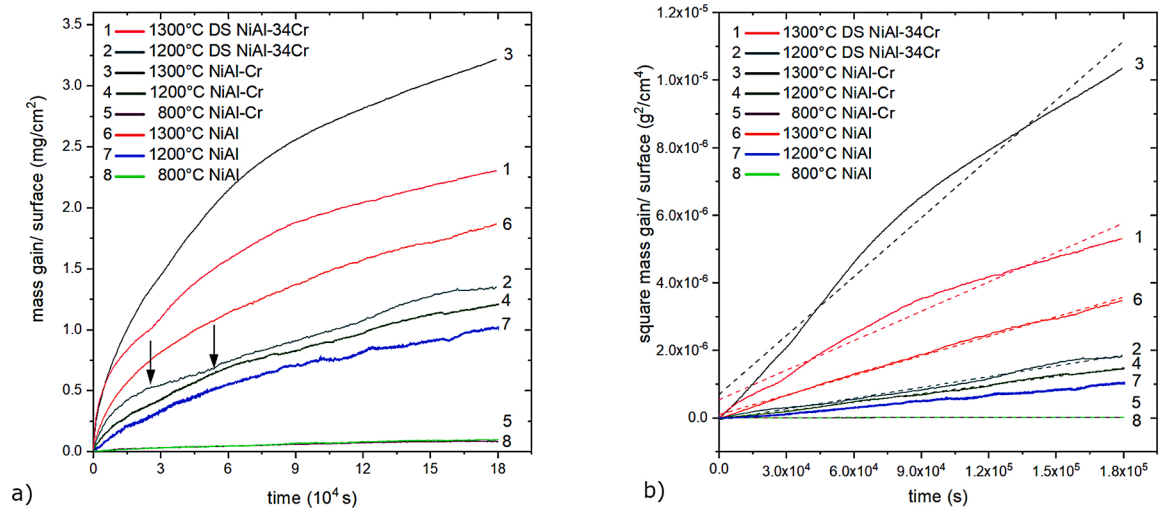


**Fig. 2.** TGA results during oxidation of NiAl-Cr, NiAl and DS NiAl-34Cr at 800 °C, 1200 °C and 1300 °C. a) mass gain. b) square of mass gain based on plot a.

temperature. After formation of oxides for about 400 min at 1200 °C, these oxides started to spall off and caused weight loss which was followed by further oxidation due to the unprotected surface. This phenomenon was less pronounced for NiAl-Cr (curve 4) and NiAl (curve 7). NiAl-Cr (curve 3) has a much higher oxidation rate at 1300 °C than DS NiAl-34Cr (curve 1) and NiAl (curve 6) which could have been caused by the fast oxidation of Cr pieces together with spallation, where the unprotected surface was oxidized subsequently. Fig. 3 shows the SEM image of the NiAl-Cr coarse composite after oxidation for 50 h in which the quantification of the overall spallation for NiAl-Cr coarse composite at temperatures of 800 °C, 1200 °C and 1300 °C could be compared. The spallation increased with temperature and mainly occurred at the interface of NiAl and Cr which will be discussed in more detail in Section 3.2.

Based on the data in Fig. 2-a the square of mass gain for each of the samples is plotted as a function of time in Fig. 2-b, in which the slope of the plot is the parabolic rate constant $K_{p,w}$ (the index "$w$" refers to the weight measurements). In this figure the dotted lines represent the average slope for the ideal parabolic behaviour. These parabolic rate constants for different samples of NiAl, NiAl-Cr coarse composite and DS NiAl-34Cr are listed in Table 1. The parabolic rate constants ($K_{p,w}$) of oxidation of NiAl, NiAl-Cr coarse composite and DS NiAl-34Cr are plotted in an Arrhenius diagram and are compared with the reported values by Brumm and Grabke in which the oxidation of pure NiAl in the temperature range of 700 °C–1400 °C is investigated [19]. This is shown in Fig. 4 where the results for NiAl and even NiAl-Cr samples show similar order of magnitude of the parabolic rate constants compared to the reported values.

In the work of Brumm and Grabke [19] during oxidation of NiAl,

**Table 1**
Parabolic oxidation rate constants for NiAl, NiAl-Cr and DS NiAl-34Cr.

| Sample | Temperature | $K_{p,w}$ ($g^2 \cdot cm^{-4} \cdot s^{-1}$) | Standard error | Adj. R-square |
|---|---|---|---|---|
| **DS NiAl-34Cr** | 1300 °C | $2.90 \times 10^{-11}$ | $2.86 \times 10^{-13}$ | 0.971 |
| **DS NiAl-34Cr** | 1200 °C | $1.06 \times 10^{-11}$ | $6.66 \times 10^{-14}$ | 0.988 |
| **NiAl-Cr** | 1300 °C | $5.81 \times 10^{-11}$ | $5.10 \times 10^{-13}$ | 0.977 |
| **NiAl-Cr** | 1200 °C | $8.48 \times 10^{-12}$ | $1.47 \times 10^{-15}$ | 0.997 |
| **NiAl-Cr** | 800 °C | $4.46 \times 10^{-14}$ | $1.29 \times 10^{-17}$ | 0.985 |
| **NiAl** | 1300 °C | $1.93 \times 10^{-11}$ | $6.30 \times 10^{-14}$ | 0.997 |
| **NiAl** | 1200 °C | $5.90 \times 10^{-12}$ | $1.21 \times 10^{-15}$ | 0.996 |
| **NiAl** | 800 °C | $5.86 \times 10^{-14}$ | $2.01 \times 10^{-17}$ | 0.979 |

formation of three oxides γ-$Al_2O_3$, θ-$Al_2O_3$ and α-$Al_2O_3$ was anticipated in which the metastable oxides γ-$Al_2O_3$ and θ-$Al_2O_3$ were formed at lower temperatures or at the early stages of oxidation and the stable α-$Al_2O_3$ oxide was formed at higher temperatures. In this work, formation of α-$Al_2O_3$ on NiAl-Cr coarse composite oxidized at 1300 °C was confirmed by XRD which is shown in Fig. 5. However, the oxides formed at 1200 °C and 800 °C were too thin and showed a strong texture effect and their further identification with XRD was not possible. Nevertheless, EBSD, confirmed the formation of α-$Al_2O_3$ on the NiAl region of the NiAl-Cr coarse composite sample during oxidation at 1200 °C.

The quasi-binary phase diagram of $Cr_2O_3$ and α-$Al_2O_3$ (Fig. 6) shows that the two components are completely soluble in each other above 909 °C. Therefore, it is expected that the oxide scale on the NiAl-Cr

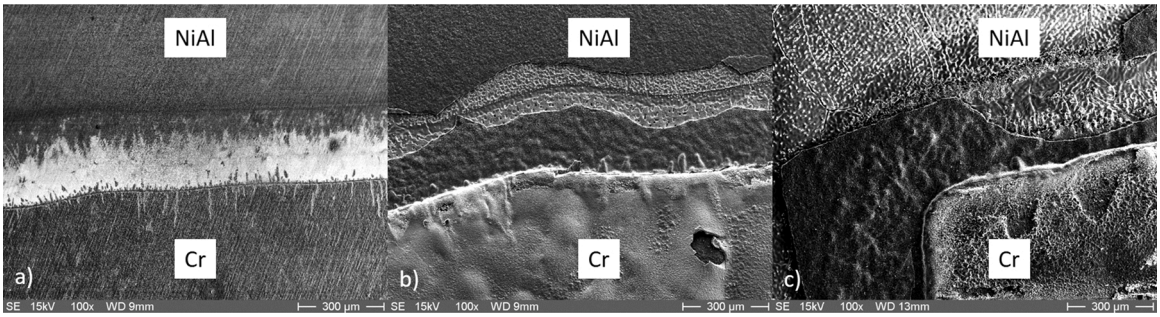


**Fig. 3.** SEM images of the oxidized surface of NiAl-Cr coarse composite after reaction in Ar/ 13 vol.% $O_2$ for 50 h. The labels denote the corresponding alloy beneath the oxide layer. a) at 800 °C. b) at 1200 °C. c) at 1300 °C.

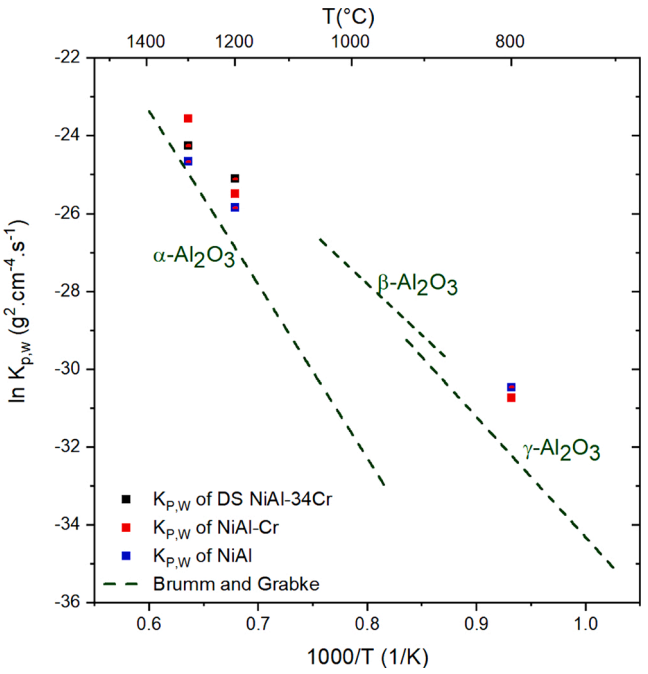


**Fig. 4.** Parabolic rate constant of oxidation of NiAl and NiAl-Cr and DS NiAl-34Cr.

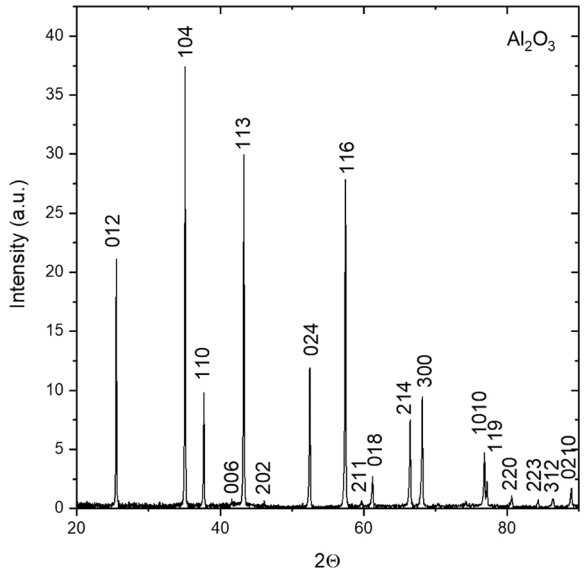


**Fig. 5.** XRD pattern of the spalled oxide from the NiAl-Cr oxidized at 1300 °C in Ar/ 13 vol.% $O_2$ for 50 h.

coarse composite interface forms a continuous solid solution of $Al_2O_3$ and $Cr_2O_3$ with corundum structure. Further investigations were performed with EDX and EBSD on the cross sections of these samples which are discussed in Section 3.2.

### 3.2. Surface and cross section investigation

Fig. 7-a shows the surface of the NiAl-Cr coarse composite sample after oxidation in the thermobalance for 50 h at 1200 °C under Ar with 13 vol.% $O_2$. The oxide layer over the NiAl substrate appears to be rather smooth compared to the oxide layer over the Cr region. As can be seen in Fig. 7-b, spallation occurred at the interface between the NiAl and Cr, which is due to the fact that the oxidation rate of Cr is much faster

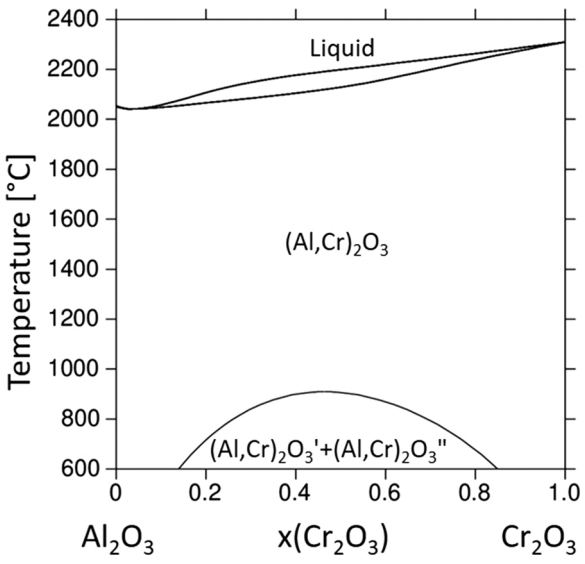


**Fig. 6.** Quasi-binary phase diagram of $Al_2O_3$ and $Cr_2O_3$ [29].

compared to the oxidation rate of NiAl. This would cause formation of voids and wrinkles at the interface due to volumetric changes. Formation of these wrinkles will lead to transformation of biaxial stress in the oxide scale into a normal stress which is perpendicular to the oxide plane and causing spallation of the oxide [23]. Different oxidation rates can also be observed from different thicknesses of the oxides of α-$Al_2O_3$ and $Cr_2O_3$ which are formed on the NiAl and Cr regions, respectively, as can be seen in Fig. 7-c and d.

In addition to TGA investigations, the oxide growth can be examined by determination of the thickness of the oxide layers using SEM images of metallographic cross-sections. These measurements provide parabolic rate constants $K_{p,t}$ (the index "$t$" refers to thickness). Table 2 provides values of $K_{p,t}$ for formation of $Al_2O_3$ layers on pure NiAl samples, for the formation of $Al_2O_3$ over the NiAl region of coarse NiAl-Cr composites as well as for oxides formed on DS NiAl-34Cr samples at temperatures of 800 °C, 1200 °C and 1300 °C. Each value represents an average of 10 measurements at different positions. In order to compare the parabolic rate constants $K_{p,t}$ ( $cm^2 \cdot s^{-1}$) of our work with the results of Brumm and Grabke [19], which were calculated based on the weight gain of the oxides $K_{p,w}$ ( $g^2 \cdot cm^{-4} \cdot s^{-1}$), the $K_{p,t}$ in this work was converted to $K_{p,w}$ by multiplying it by $\rho_a^2$. Where $\rho_a$ is the apparent density of the oxide layers.

The apparent densities were estimated based on the experimental mass gain, the surface area and the average thickness of the $Al_2O_3$ layer formed at each isothermal condition on different samples of NiAl, NiAl-Cr coarse composite and DS NiAl-34Cr (Table 2). Please note that these apparent density values are smaller compared to the density of a compact α-$Al_2O_3$ ($\rho = 3.89\ g \cdot cm^{-3}$) which is due to the high porosity of the oxide layers. In addition, for the simplicity of the approximation, the Cr substrate area in NiAl-Cr coarse composites and DS NiAl-34Cr is not taken into account and the substrate surface is considered as complete NiAl. The Cr substrate included less than 4% of the surface in NiAl-Cr. This procedure can be further justified by the experimental findings during the oxidation of DS NiAl-34Cr in which practically pure $Al_2O_3$ is formed, as will be discussed later in Section 3.2.4.

In Fig. 9 the converted values are shown on the right axis and they are compared with the parabolic rate constants ($K_{p,w}$) reported by Brumm and Grabke on the left axis [19]. The results show reasonable agreement with the same order of magnitude of the parabolic rate constants. To calculate the error bars each oxide thickness was measured 10 times and the standard deviation was calculated based on the average measured value.

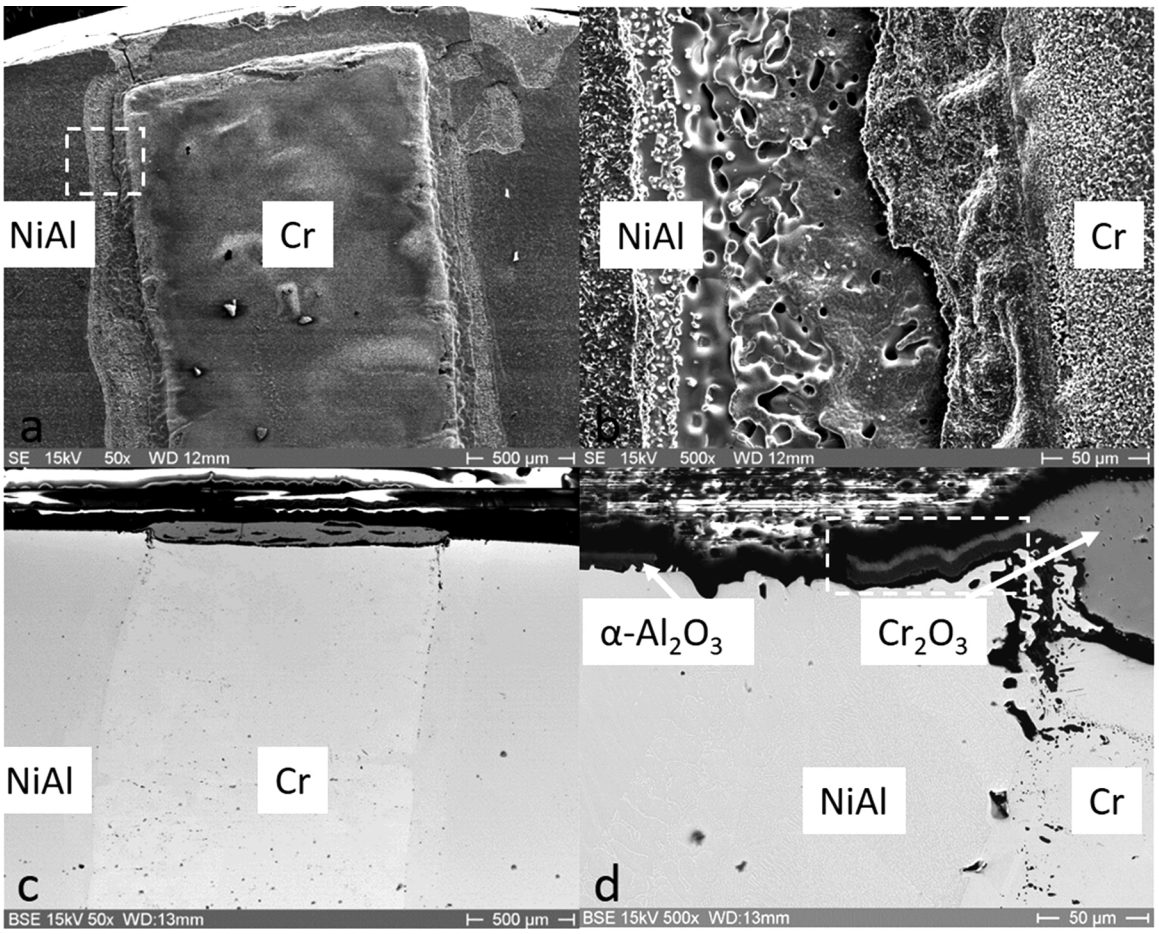


**Fig. 7.** NiAl-Cr oxidized at 1200 °C and Ar/ 13 vol.% $O_2$ for 50 h. a) Surface image. b) Enlarged image of a: Spallation at the interface of NiAl-Cr. c) Cross section image. d) Enlarged image of c: Interface of NiAl-Cr (for the discussion of the dashed box see Section 3.2.2).

**Table 2**
Parabolic oxidation rate constant $K_{p,t}$ for NiAl, NiAl-Cr and DS NiAl-34Cr and density of the oxide layers.

| Sample | Temperature | $K_{p,t}$ $(cm^2 \cdot s^{-1})$ | $\rho_a$ of $Al_2O_3$ $(g \cdot cm^{-3})$ |
|---|---|---|---|
| **DS NiAl-34Cr** | 1300 °C | $9.74 \times 10^{-12}$ | 1.531 |
| **DS NiAl-34Cr** | 1200 °C | $2.33 \times 10^{-12}$ | 2.146 |
| **NiAl-Cr** | 1300 °C | $1.65 \times 10^{-11}$ | 1.482 |
| **NiAl-Cr** | 1200 °C | $3.93 \times 10^{-12}$ | 1.439 |
| **NiAl-Cr** | 800 °C | $1.16 \times 10^{-14}$ | 1.790 |
| **NiAl** | 1300 °C | $7.09 \times 10^{-12}$ | 1.649 |
| **NiAl** | 1200 °C | $2.80 \times 10^{-12}$ | 1.408 |
| **NiAl** | 800 °C | $3.24 \times 10^{-14}$ | 1.255 |

### 3.2.1. Oxidation of NiAl-Cr coarse composite at 800 °C

In Fig. 10 the EDX map of the region around the joint between NiAl and Cr in the NiAl-Cr coarse composite is shown after oxidation in the thermobalance at 800 °C for 50 h under Ar with 13 vol.% $O_2$. This image shows NiAl on the left and Cr on the right. The element maps of O, Cr, Ni and Al are shown, respectively.

The oxide scales which formed above the NiAl region were too thin and could not be identified with XRD or EBSD. However, the oxide above the Cr region was identified as $Cr_2O_3$ by EBSD.

Oxygen seems to be detected by EDX in the substrate where only pure Cr was expected (Fig. 10). As no internal oxidation was anticipated in this region the enrichment of the Cr region with oxygen due to diffusion is not presumed. The apparent detection of oxygen is due to the overlapping of the chromium $L_\alpha$ line with the oxygen $K_\alpha$ line since they are very close to each other, with energies of 0.572 and 0.525 KeV, respectively. Similar observations have been reported by Peng et al. [24].

In the region between NiAl and Cr, dendrites are observed. These dendrites are formed during the casting process in the arc-melting device, as described in Section 2.1. When molten NiAl is cast over solid chromium, then some Cr dissolves in the melt because the temperature is above the melting point of NiAl but below the melting point of Cr, as can be seen from phase diagram in Fig. 11. Due to the short duration of this process, the Cr-enriched melt is confined to a small region next to the solid Cr. As the temperature decreases below the liquidus line, Cr dendrites are formed and finally when the eutectic temperature is approached a eutectic microstructure is formed in the region of the NiAl-Cr joint, as shown in Fig. 12.

### 3.2.2. Oxidation of NiAl-Cr coarse composite at 1200 °C

The oxidation at 1200 °C and 1300 °C took place in the subsolidus region of the NiAl-Cr samples. However, the dendrite structures which are observed at 800 °C can coarsen during 50 h at 1200 °C and 1300 °C. For this reason the NiAl and Cr interface at these two relatively high temperatures appears differently compared to those formed at 800 °C.

As can be seen in Fig. 7-d, at the interface between Cr and NiAl, an oxide of $(Al,Cr)_2O_3$ is formed which can be noticed within the dashed box. The enlarged image of the dashed box is shown in Fig. 8. The oxide in the SEM image appears brighter moving from the metal surface to the gas surface. This can be an indication of a decrease in the amount of Al with lower atomic number and an increase in Cr content. Please note that the $Al_2O_3$-rich layer is detached from the substrate and therefore a

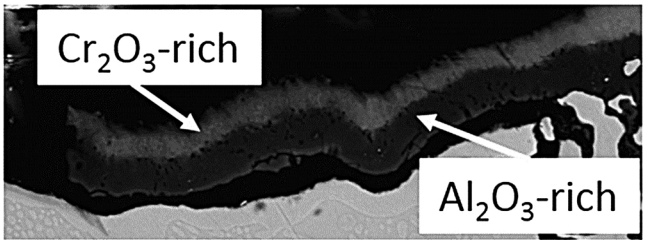


**Fig. 8.** Enlarged image of the dashed box shown in Fig. 7-d.

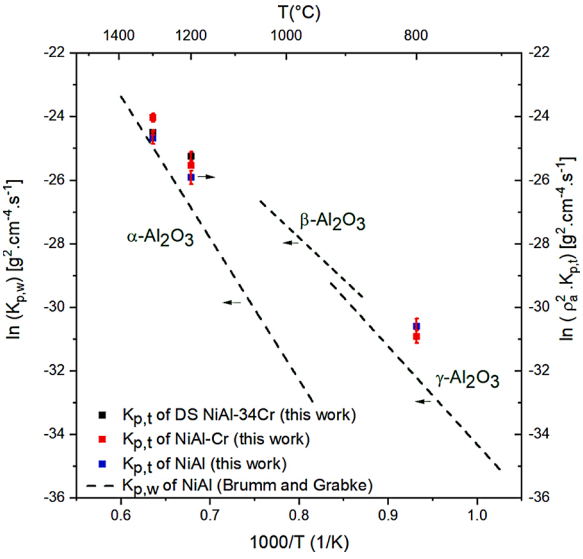


**Fig. 9.** Arrhenius diagram of oxidation of NiAl-Cr, DS NiAl-34Cr and NiAl.

small gap appears between the oxide and the substrate in Fig. 8. Further investigation of the identical interface area with EDX and EBSD showed that α-$Al_2O_3$ was formed on top of the NiAl region and $Cr_2O_3$ was formed above the Cr region. These oxides were investigated with EDX mapping and are shown in Fig. 13. Oxygen can be seen at the surface of the sample where oxidation happened and there is a high concentration of Al on the surface at the interface between NiAl and Cr.

The processed image from EDX and EBSD which is shown in Fig. 14 only confirmed the formation of α-$Al_2O_3$ at the interface of NiAl and Cr after oxidation at 1200 °C. This was in contradiction with the initial indications from the SEM image for formation of a mixed $(Al,Cr)_2O_3$ oxide. The investigation was continued further at higher temperatures where the oxide layers are much thicker which allows better investigation of the formed oxides.

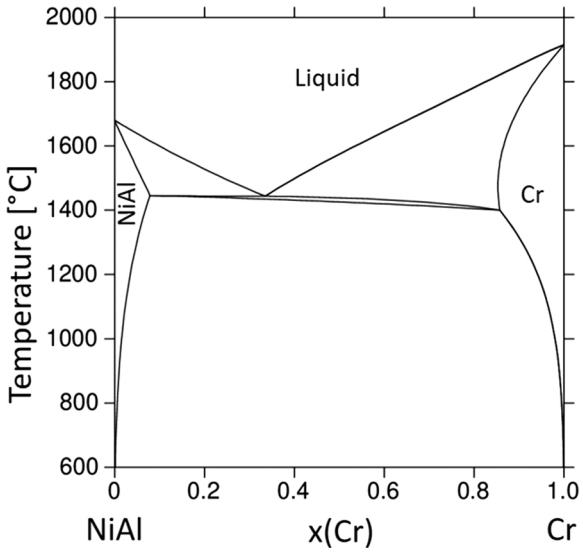


**Fig. 11.** Calculated section NiAl-Cr.

### 3.2.3. *Oxidation of NiAl-Cr coarse composite at 1300 °C*

The EDX analysis for a NiAl-Cr sample oxidized for 50 h at 1300 °C under Ar with 13 vol.% $O_2$ is shown in Fig. 15. When the NiAl-Cr coarse composite is exposed to high oxygen activities at 1300 °C, then an oxide scale forms on top of the metals which consists of $Cr_2O_3$ and α-$Al_2O_3$. As shown in the processed image from EDX and EBSD in Fig. 16, the results indicate the formation of a mixed oxide in which the composition varies from the metal surface to the gas surface. Even though, the outer layer of the oxide is mainly $Cr_2O_3$-rich, as can be seen from the EDX maps of the element distribution in Fig. 15, some Al also exists in the $Cr_2O_3$-rich oxide. The same is true for the existence of Cr in the inner oxide layer which is mainly $Al_2O_3$-rich. Please note, due to methodological reasons, in the combined EDX and EBSD results, it is not possible to clearly indicate the continuous change in Al and Cr content in Fig. 16. Rather, it is shown with two different colors. However it does not imply to two distinct oxide layers but a continuous solid solution in which the yellow region is Cr-rich and the blue region is Al-rich. The reason for formation of the gradient in composition of the oxide can be explained as follows.

The parabolic rate constant of Cr oxidation at 1300 °C is about five orders of magnitude higher than that of NiAl oxidation [25]. Therefore,

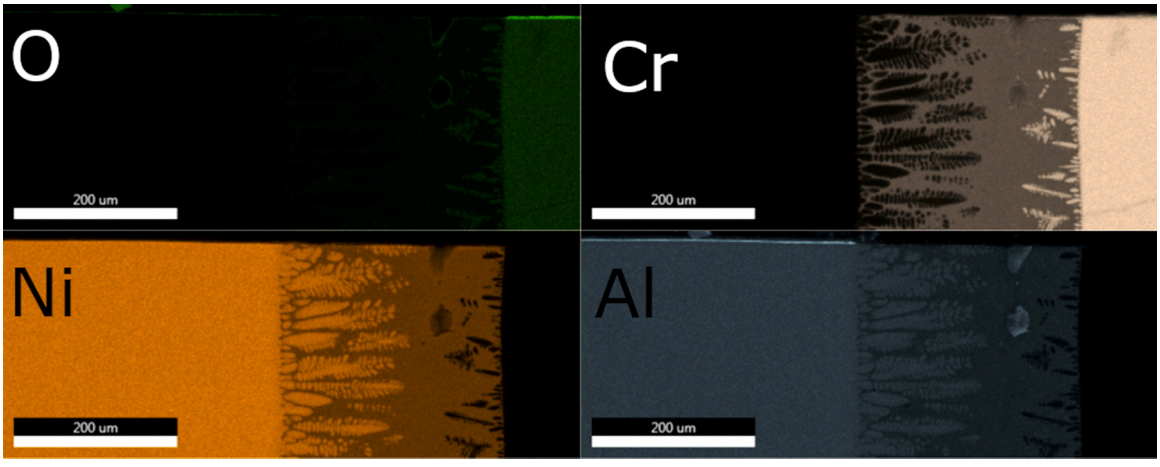


**Fig. 10.** EDX map of the region around the joint between NiAl and Cr in NiAl-Cr oxidized at 800 °C in Ar/ 13 vol.% $O_2$ for 50 h.

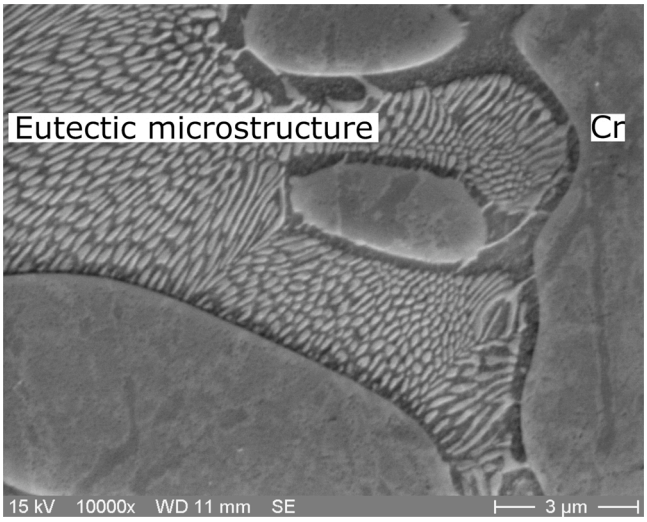


**Fig. 12.** Microstructure of the solidified NiAl in the vicinity of Cr rod after annealing at 800 °C for 50 h.

the parabolic rate constant for the mixed oxide forming over the region between NiAl and Cr is a continuous function of the composition. The transport properties of the mixed oxide also change strongly with composition. The interdiffusion coefficient of $Cr_2O_3$-$Al_2O_3$ as a function of composition is investigated in temperature range of 1400 °C–1520 °C, in the work from Atarashiya et al. [26]. The investigation indicates that at high Cr-contents the interdiffusion of aluminium and chromium are by one order of magnitude higher than at high Al-contents. This behaviour causes a relatively thick oxide layer to be formed over chromium, which consists of almost pure $Cr_2O_3$ and is shown in yellow color in Fig. 16. Over the NiAl matrix at a sufficient distance from the interface between NiAl and Cr, only a thin oxide scale is formed consisting of

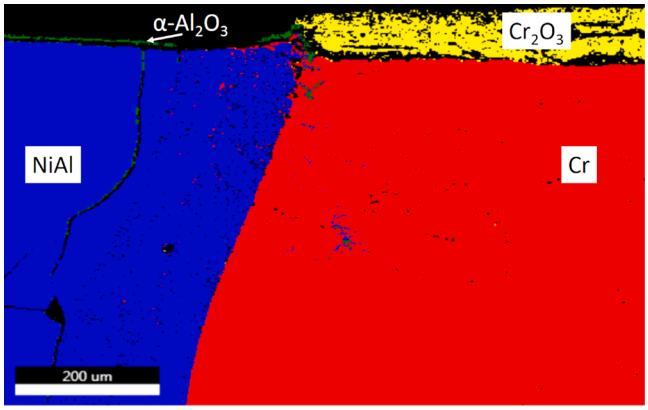


**Fig. 14.** Phase image of NiAl-Cr oxidized at 1200 °C.

almost pure $Al_2O_3$ which is shown in blue color.

In the vicinity of the interface of NiAl and Cr, due to the faster diffusion in the high Cr-content region, Cr diffuses over the $Al_2O_3$ and causes formation of an oxide layer in which the composition changes from almost pure $Al_2O_3$ (blue) in contact with the metal, to almost pure $Cr_2O_3$ (yellow) in contact with the gas. The Cr content in the oxide scale also decreases in the direction from the interface towards the NiAl.

As shown in the Ellingham diagram in Fig. 17, the Gibbs energy of formation of $Al_2O_3$ is much lower than that of $Cr_2O_3$ and NiO which means it is more stable than $Cr_2O_3$ and it would be the first oxide to be formed at the interface. Later, when there is deficiency of Al, Cr will start oxidizing, as the $Cr_2O_3$ activity increases.

A schematic view of the oxide formation near the interface between NiAl and Cr is presented in Fig. 18. The concentration of Cr increases while getting closer to the Cr region and also it increases in direction of the surface of the oxide. Red arrows show the directions of increasing Cr content in the $(Al,Cr)_2O_3$ solid solution.

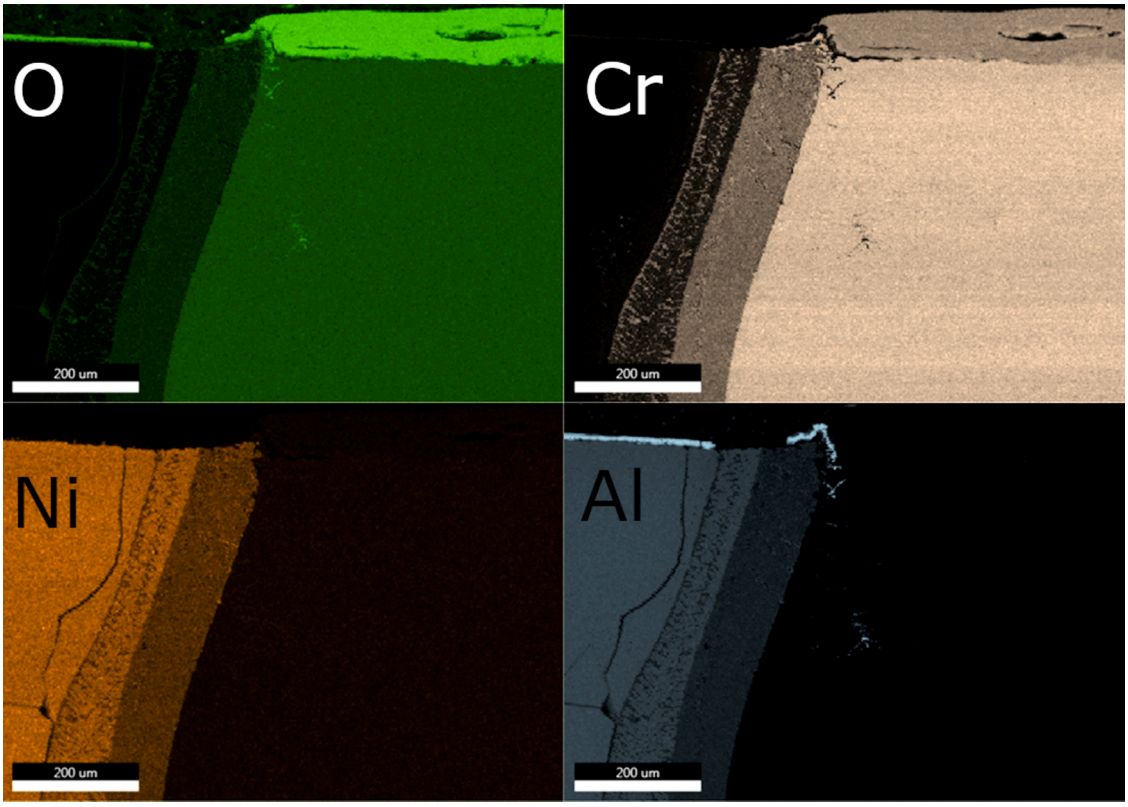


**Fig. 13.** EDX map of interface of NiAl and Cr in NiAl-Cr oxidized at 1200 °C.

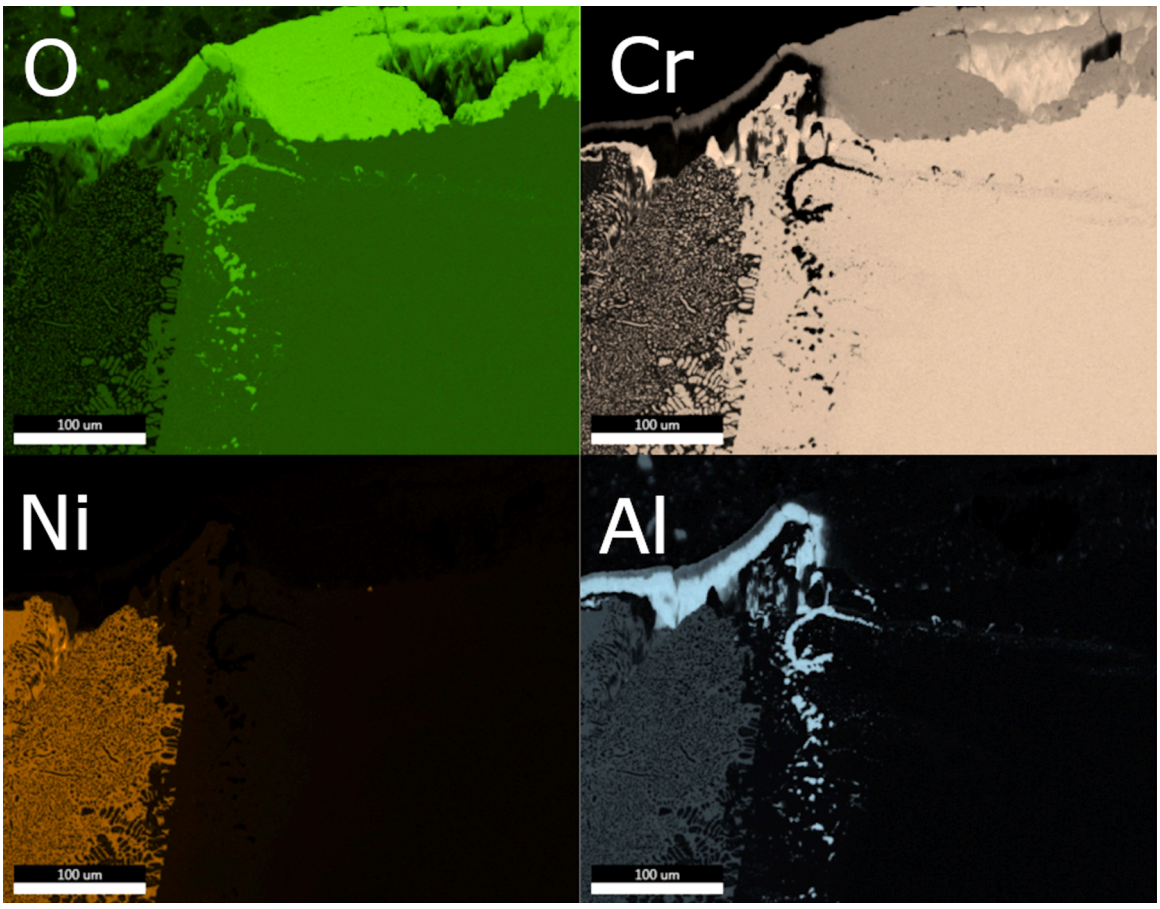


**Fig. 15.** EDX map of interface of NiAl and Cr in NiAl-Cr oxidized at 1300 °C.

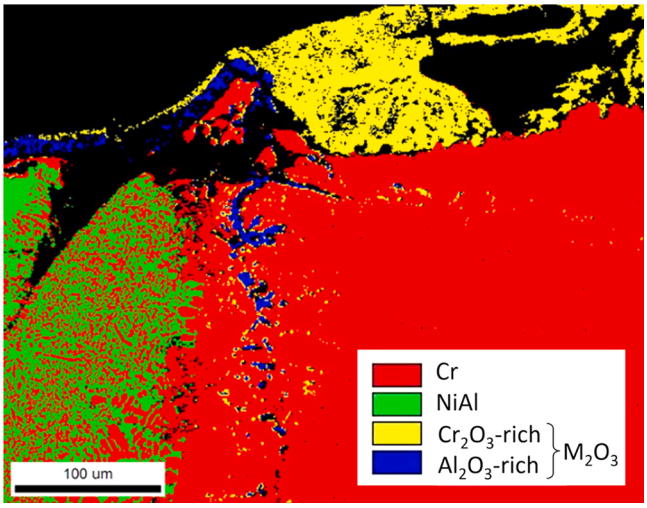


**Fig. 16.** Phase image of NiAl-Cr oxidized at 1300 °C.

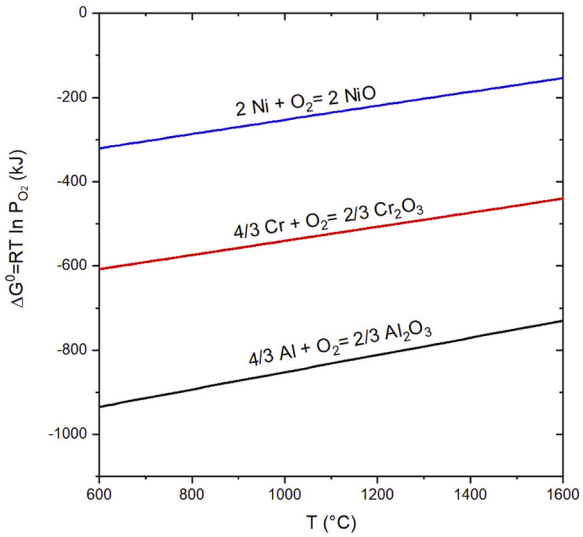


**Fig. 17.** Ellingham diagram of $Al_2O_3$ and $Cr_2O_3$ and NiO.

This means that the composition of $(Al,Cr)_2O_3$ changes simultaneously in two different directions. This makes it challenging to calculate the composition of the oxide at a specific distance from the metallic surface. Without having the exact composition at the interface further calculation of activities and the driving forces for formation of oxides are not possible.

During the process of oxidation the sample is under a strong oxygen potential gradient. On the surface, the sample is in contact with the gas atmosphere with an oxygen activity of $a_{O_2} = 0.13$, while inside the metallic composite, the oxygen activity is many orders of magnitude lower. These changing local equilibria are discussed below by means of several thermodynamic diagrams which have been calculated with the thermodynamic database [17] which is mentioned in the introduction.

The potential-composition diagram for the Al-Cr-O system at 1300 °C is plotted in Fig. 19-a. It can be seen that at any oxygen partial pressure higher than $\log(p_{O_2}) = -16$ bar the $(Al,Cr)_2O_3$ mixed oxide with the corundum structure is stable for all compositions. In equilibrium with


**Fig. 18.** Schematic view of NiAl-Cr with oxide scales. Arrows show direction of increasing of Cr concentration.

Cr-Al alloys the oxide has high chromium concentrations only within a small range where $\log(p_{O_2})$ is between −16 and −17. At even lower oxygen partial pressures the oxide consists of almost pure $Al_2O_3$.

As shown in Fig. 19-b in the system Ni-Al-O at high oxygen partial pressures $Al_2O_3$, NiO and the spinel phase ($NiAl_2O_4$) are the stable oxides. However, in the oxidation experiments only $Al_2O_3$ was formed, as confirmed by EBSD and XRD. An explanation can be given by means of Fig. 19-b which shows that pure $Al_2O_3$ is the only oxide being in equilibrium with NiAl. Therefore, it forms first and since nickel is practically insoluble in $Al_2O_3$ it cannot diffuse through the oxide layer in order to form spinel or even NiO on the surface of the sample.

While Fig. 19-a provides insight into the oxidation behaviour of the Cr-based alloy, and Fig. 19-b gives the respective information for the matrix (NiAl) of our composite material, we now proceed to sections through the quaternary system where the oxidation of the composite can be discussed. In Fig. 20-a a section through the system Ni-Al-Cr-O is shown at 1300 °C and $\log(p_{O_2})$= −24. Under these conditions several phase equilibria are possible, depending on the mixing ratio of the metallic components. The green tie-lines between the NiAl phase and the Cr-rich alloy phase represent equilibria which can be found in the interior of the composite sample at the junction of the corresponding alloys at sufficient distance from the surface (and the oxide layer on it). The tie-triangle between NiAl, (Cr), and $Al_2O_3$ represents the equilibrium at the junction between NiAl and (Cr) directly below the oxide layer at the surface of the sample. The narrow two-phase regions $Al_2O_3$-NiAl and $Al_2O_3$-(Cr) represent the equilibria between the oxide layer and the corresponding alloys at a certain distance from the NiAl-Cr junction.

In Fig. 20-b the section through the quaternary system is given for the same temperature but at a higher oxygen potential, $\log(p_{O_2})$=−21. It can be seen that now the matrix phase NiAl is no longer stable and instead only a Ni-rich and a Cr-rich alloy phase exist. Compared to Fig. 20-a these alloys have less solubility for aluminium. The oxide forming on these alloys is in both cases almost pure $Al_2O_3$.

If the oxygen partial pressure is further increased towards log $(p_{O_2})$=−16 the diagram remains similar to Fig. 20-b except that the mixed oxide $(Al,Cr)_2O_3$ extends from the $Al_2O_3$-corner along the right axis of the diagram almost down to the Cr-corner (Fig. 20-c).

Finally, a small effect should be addressed, which occurs during the oxidation of the NiAl-Cr composite. A closer look at Figs. 15 and 16 reveals that oxide particles have formed within the Cr-rich alloy at a short distance from the contact area between the two alloys. The mechanism of internal oxidation can be assumed to be the cause of their formation. In the previous discussion of Figs. 19 and 20 it was shown that in the equilibrium between almost pure chromium and its oxide there is a much higher oxygen activity than in the equilibrium between NiAl and $Al_2O_3$. Therefore, the contact zone between NiAl and Cr is located within an oxygen potential gradient, which causes a (small) oxygen flow from the Cr side to NiAl. On the other hand, small amounts of NiAl can dissolve in chromium, creating an aluminium stream that diffuses in opposite direction of the oxygen stream. In the region where the concentrations of Al and O exceed the solubility product of $Al_2O_3$ in chromium, the oxide particles are precipitated.

### 3.2.4. *Oxidation of DS NiAl-34Cr at 1200 °C and 1300 °C*

In Fig. 21-a and b, cross-section SEM images of DS NiAl-34Cr samples are shown after 50 h of oxidation in Ar/ 13 vol.% $O_2$ at 1200 °C and 1300 °C, respectively. In both cases an oxide layer of almost pure $Al_2O_3$ was formed on the samples, as found by EPMA. It can be seen that the oxide layer is largely detached from the underlying alloys.

The formerly fibrous composite has transformed during the heat-treatment into a nodular microstructure. This effect is shown by the fact that a section in any direction through the sample reveals the same microstructure within the region of the NiAl + Cr composite as shown in Fig. 21. Furthermore, between the NiAl + Cr composite and the oxide scale a layer of Cr-rich alloy has formed. The EPMA analysis showed the Cr content of 96.81 at.% and 94.58 at.% at 1200 °C and 1300 °C, respectively. Formation of this Cr-rich region has caused the spallation due to different thermal expansion coefficients or deteriorating the adhesion to the $Al_2O_3$ oxide scale. The composition of this Cr-rich region is shown in Table 3. Similar observations of formation of the Cr-rich region below the oxide scale were reported in the literature in which

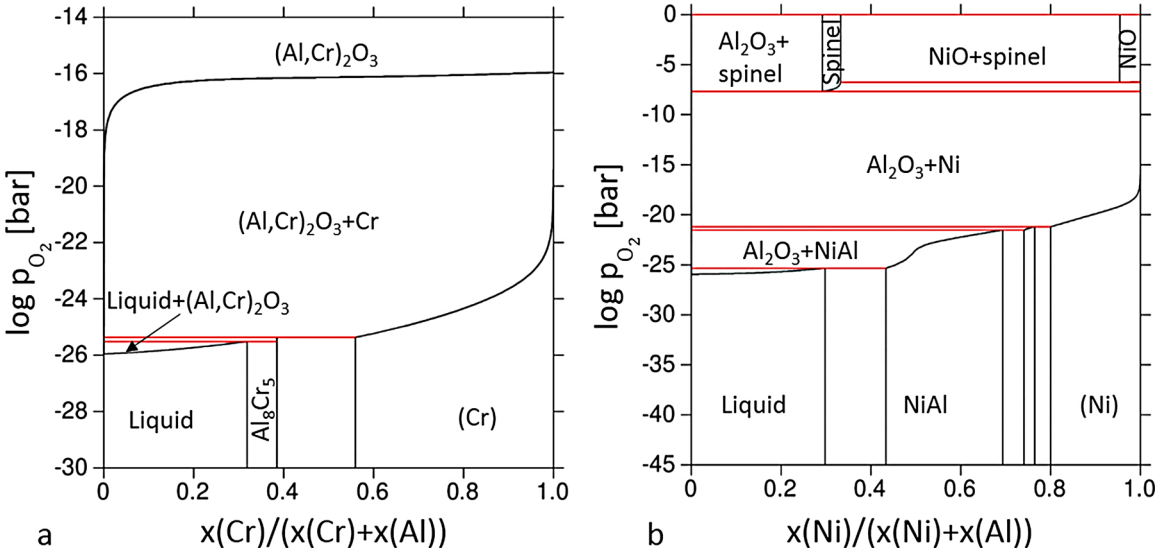


**Fig. 19.** Calculated stability diagram as a function of oxygen partial pressure at 1300 °C. a) in the Al-Cr-O system. b) in the Al-Ni-O system.

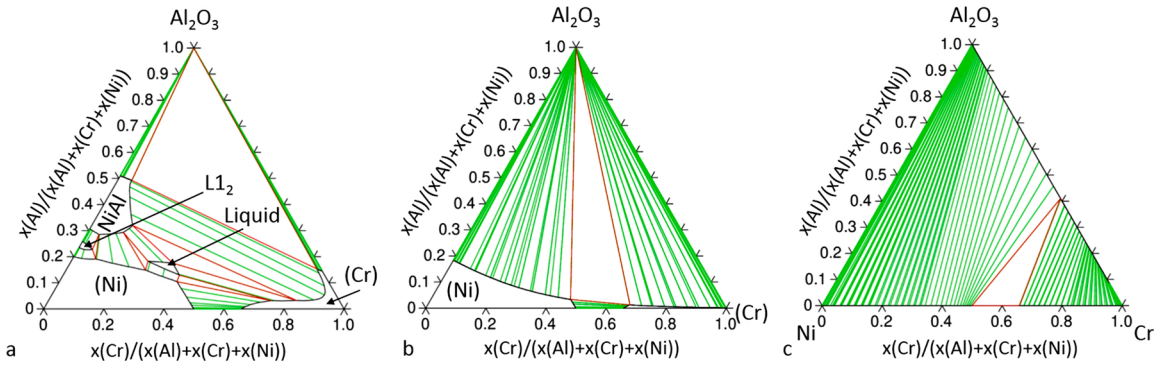


**Fig. 20.** Section through the system Ni-Al-Cr-O at 1300 °C in: a) log ($p_{O_2}$) = −24. b) log ($p_{O_2}$) = −21. c) log ($p_{O_2}$)= −16.

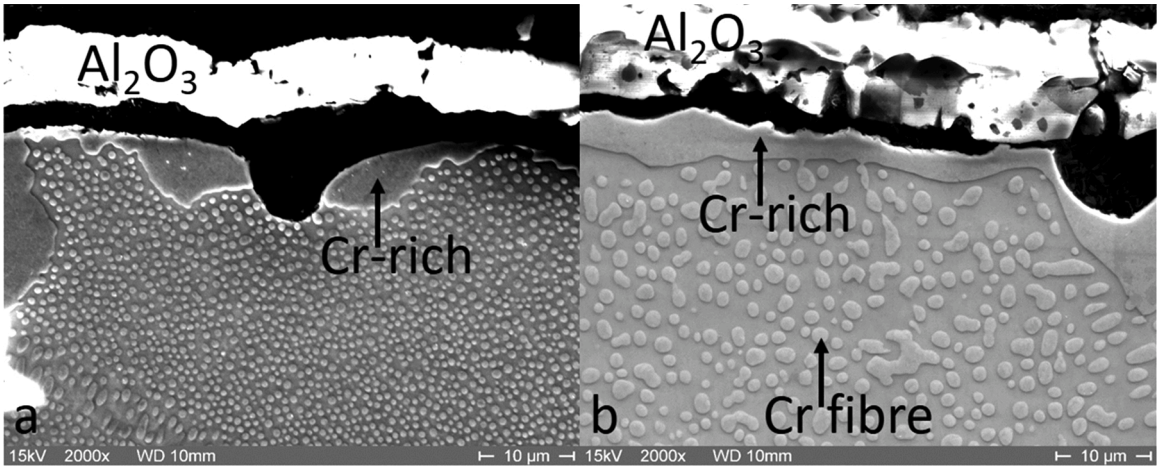


**Fig. 21.** Cross section of DS NiAl-Cr oxidized under Ar/ 13 vol.% $O_2$ for 50 h. a) at 1200 °C. b) at 1300 °C.

it was assumed that formation of the Cr-rich region is due to rejection of Cr from the growing oxide scale and the low solubility of Cr in the NiAl matrix [24,27,28]. However, in view of Fig. 20-a the influence of the Ni concentration on the solubility of Cr in NiAl seems to be too small than to account for this effect. A better explanation can be given if the alloys are approached by higher oxygen activities than those of the NiAl/$Al_2O_3$ equilibrium. Fig. 21-a and b show that the oxide layers are not dense and that they are detached from the alloys which permits contact with the gas leading to increased oxygen activities in a zone next to the alloy surface. If the oxygen activities approach a level close to that of Fig. 20-b then the NiAl phase can no longer exist in that zone and a rim of Cr-rich alloy is formed instead. In the interior of the sample the oxygen activities are still low enough to keep NiAl stable.

Since almost pure $Al_2O_3$ is formed during the oxidation, the metallic phases must become enriched with nickel. According to Fig. 20-a, some Ni can dissolve in the NiAl matrix but a higher amount can be expected in the Cr-rich alloy where the solubility is about 35 at.% Ni at 1300 °C. The composition of the alloy phases shown in Fig. 21-b have been investigated by electron-probe microanalysis and the results are shown in Table 3. Surprisingly, the expected increased Ni concentrations in the Cr-rich alloys were not found. However, due to the fact that the fibres are in the order of nm scale, the EPMA results for the matrix and the fibres are not accurate. The relatively high Cr content (6.99 at.%) in the matrix indicates the overlapping of results from matrix and the fibres.

**Table 3**
Microprobe analysis of Cr-rich region, fibres and matrix in oxidized DS NiAl-34Cr at 1300 °C after 50 h.

| Element | Element distribution in the Cr-rich region (at. %) | Element distribution in the fibres (at.%) | Element distribution in the matrix (at.%) |
|---|---|---|---|
| **Al** | 2.48 | 3.32 | 41.87 |
| **Cr** | 94.58 | 92.16 | 6.99 |
| **Ni** | 2.94 | 4.53 | 51.14 |

### 3.3. Oxidation of NiAl-Mo

Oxidation of directionally solidified NiAl-Mo was already investigated by Brady et al. [15] where the effect of the Mo dispersion size was investigated in both dry and wet conditions at 900 °C. The samples showed good oxidation resistance via $Al_2O_3$ formation in dry air.

To identify the oxides formed at the interface between NiAl and Mo, a NiAl-Mo coarse composite was oxidized at 800 °C for 50 h under Ar atmosphere with 13 vol.% $O_2$. As can be seen in Fig. 22, there is a huge mass loss during the oxidation of NiAl-Mo. The reason is the formation of volatile Mo oxide species. The Mo wire is oxidized and forms a yellow powder (Fig. 23). It was analysed by XRD and showed formation of $Al_2Mo_3O_{12}$ and $NiMoO_4$ (Fig. 24). These phases form by reaction of $MoO_3$ with $Al_2O_3$ and NiO, respectively. Formation of this powder left a hole in the sample which makes it challenging to further investigate the interface.

Fig. 25 shows the partial pressures of gaseous $MoO_x$ species over solid (and liquid) molybdenum oxides as a function of the oxygen partial pressure at 800 °C. It can be seen that under the conditions of the oxidation experiment the total partial pressure of Mo-species is at about 0.1 bar which leads to a rapid volatilization of the oxides. For further investigation of the interface, one could decrease the oxygen partial pressure down to $10^{-20}$ bar so that partial pressure of $MoO_2$ gets higher than $MoO_3$ and presumably prevents the formation of the powder at the interface.

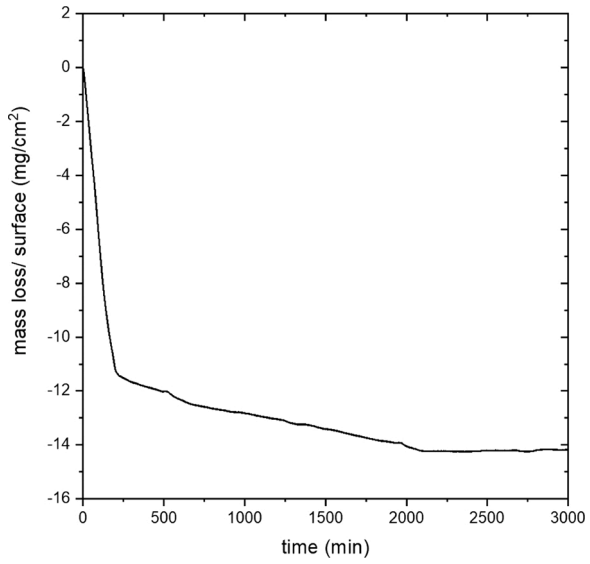


**Fig. 22.** Mass loss during oxidation of NiAl-Mo at 800 °C, Ar/ 13 vol.% $O_2$.

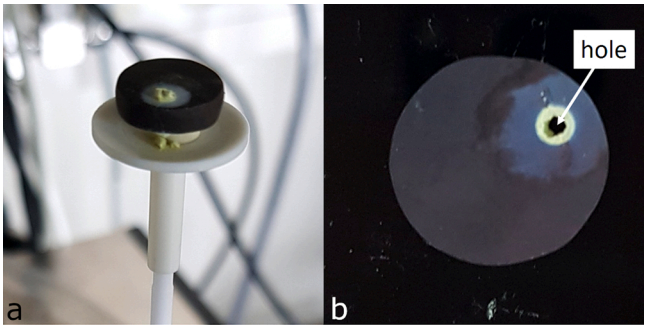


**Fig. 23.** NiAl-Mo oxidized at 800 °C for 50 h.

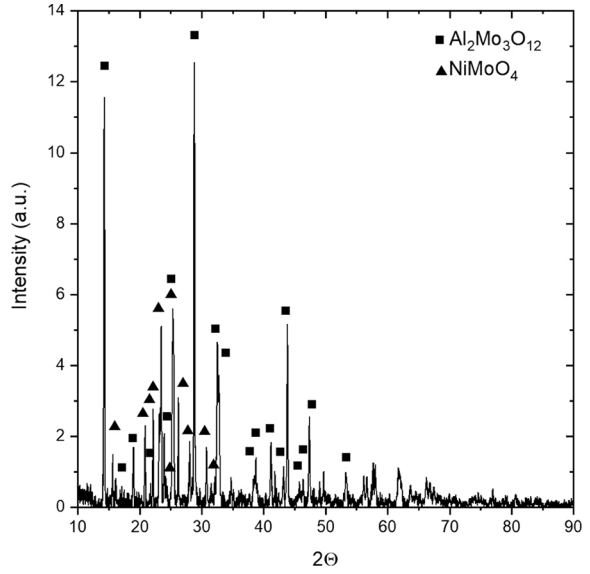


**Fig. 24.** XRD pattern of the residuals of oxides at the vicinity of Mo in NiAl-Mo alloy after oxidation at 800 °C for 50 h in Ar/ 13 vol.% $O_2$.

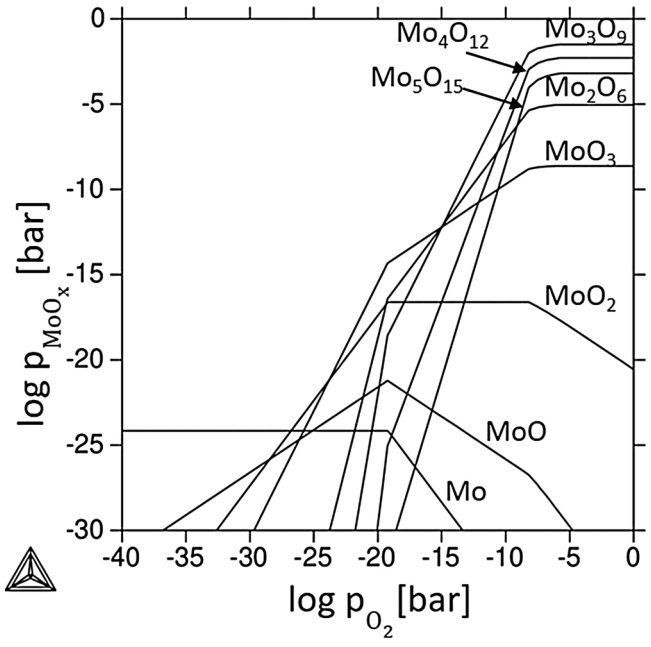


**Fig. 25.** Partial pressure of $MoO_x$ vs. oxygen partial pressure at 800 °C.

## 4. Conclusion

Coarse composites of NiAl-Cr and NiAl-Mo were produced and oxidized at defined oxygen activities and isothermal condition. During oxidation of NiAl-Cr a continuous solid solution of $(Al,Cr)_2O_3$ was formed at the interface of NiAl and Cr in which the composition changed from almost pure $Al_2O_3$ near the NiAl matrix to almost pure $Cr_2O_3$ in contact with the gas while pure $Cr_2O_3$ and $Al_2O_3$ were formed on Cr region and NiAl region, respectively. This oxide layer was to some extent protective.

At 1200 °C NiAl has the best oxidation resistance compared to NiAl-Cr coarse composite and DS NiAl-34Cr. At this temperature mass gain fluctuation due to spallation of oxide scale is seen during oxidation of DS NiAl-34Cr which led to a higher oxidation rate compared to the NiAl-Cr coarse composite. This spallation is mainly caused by Cr-rich region formed between the oxide scale and the substrate surface. The NiAl-Cr coarse composite does not show huge spallation of oxide scales at 1200 °C.

At 1300 °C the NiAl-Cr coarse composite has a higher oxidation rate compared to DS NiAl-34Cr and pure NiAl, which could be caused by faster oxidation of Cr pieces and spallation at the interface of NiAl and Cr.

Oxidation of NiAl-Mo on the other hand, was completely corrosive and volatile oxides were formed which evaporated from the surface and left a hole in the sample. The residual of the powder showed formation of $Al_2Mo_3O_{12}$ and $NiMoO_4$.

Calculation of potential phase diagram presenting the partial pressure of $MoO_x$ species with respect to oxygen partial pressure showed that at high oxygen activities the oxides which will form have high volatilization which is the main reason for the destructive oxidation.

## Data availability

The data required to support the findings of this study are available from the corresponding author upon request.

## CRediT authorship contribution statement

**Golnar Geramifard:** Conceptualization, Investigation, Writing - original draft. **Camelia Gombola:** Investigation, Writing - review &

editing. **Peter Franke:** Investigation, Writing - review & editing. **Hans J. Seifert:** Supervision, Writing - review & editing.

## Declaration of Competing Interest

The authors declare no conflict of interest. The funders had no role in the design of the study; in the collection, analyses, or interpretation of data; in the writing of the manuscript, or in the decision to publish the results.

## Acknowledgments

This work is financially supported by the Initiative and Networking Fund of the Helmholtz Association (VH-KO-610). The authors thank Dr. Martin Steinbrück for the support with the oxidation experiments, Dr. Jan Hoffmann for the EBSD measurements and Dr. Harald Leiste for the great help with the XRD measurements (all colleagues from IAM-AWP).

## Appendix A. Supplementary data

Supplementary material related to this article can be found, in the online version, at doi:https://doi.org/10.1016/j.corsci.2020.108956.

## References

[1] R.D. Noebe, R.R. Bowman, M.V. Nathal, Physical and mechanical properties of the B2 compound NiAl, Int. Mater. Rev. 38 (1993) 193–232, https://doi.org/10.1179/imr.1993.38.4.193.
[2] F. Ebrahimi, S. Shrivastava, Brittle-to-ductile transition in NiAl single crystal, Acta Mater. 46 (1998) 1493–1502, https://doi.org/10.1016/S1359-6454(97)00370-4.
[3] C. Seemüller, M. Heilmaier, T. Haenschke, H. Bei, A. Dlouhy, E.P. George, Influence of fiber alignment on creep in directionally solidified NiAl–10Mo in-situ composites, Intermetallics 35 (2013) 110–115, https://doi.org/10.1016/j.intermet.2012.12.007.
[4] L. Hu, G. Zhang, W. Hu, G. Gottstein, S. Bogner, A. Bührig-Polaczek, Tensile creep of directionally solidified NiAl–9Mo in situ composites, Acta Mater. 61 (2013) 7155–7165, https://doi.org/10.1016/j.actamat.2013.08.017.
[5] H. Bei, E.P. George, Microstructures and mechanical properties of a directionally solidified NiAl–Mo eutectic alloy, Acta Mater. 53 (2005) 69–77, https://doi.org/10.1016/j.actamat.2004.09.003.
[6] C.Y. Cui, Y.X. Chen, J.T. Guo, D.X. Li, H.Q. Ye, Preliminary investigation of directionally solidified NiAl–28Cr–5.5Mo–0.5Hf composite, Mater. Lett. 43 (2000) 303–308, https://doi.org/10.1016/S0167-577X(99)00278-5.
[7] J.L. Walter, H.E. Cline, The effect of solidification rate on structure and high-temperature strength of the eutectic NiAl-Cr, Metall. Mater. Tran. B 1 (1970) 1221–1229, https://doi.org/10.1007/bf02900234.
[8] D.R. Johnson, X.F. Chen, B.F. Oliver, Processing and mechanical properties of in-situ composites from the NiAlCr and the NiAl(Cr,Mo) eutectic systems, Intermetallics 3 (1995) 99–113, https://doi.org/10.1016/0966-9795(95)92674-O.
[9] Z. Shang, J. Shen, L. Wang, Y. Du, Y. Xiong, H. Fu, Investigations on the microstructure and room temperature fracture toughness of directionally solidified NiAl–Cr(Mo) eutectic alloy, Intermetallics 57 (2015) 25–33, https://doi.org/10.1016/j.intermet.2014.09.012.
[10] K. Wefers, C. Misra, Oxides and Hydroxides of Aluminum, Alcoa Research Laboratories, 1987.
[11] R. Klumpes, C.H.M. Maree, E. Schramm, J.H.W. de Wit, The influence of chromium on the Oxidation of ß-NiAl at 1000 °C, Mater. Corros. 47 (1996) 619–624.
[12] J.C. Yang, E. Schumann, I. Levin, M. Rühle, Transient oxidation of NiAl, Acta Mater. 46 (1998) 2195–2201.
[13] H.J. Grabke, Oxidation of NiAl and FeAl, Intermetallics 7 (1999) 1153–1158, https://doi.org/10.1016/S0966-9795(99)00037-0.
[14] H.J. Grabke, M.W. Brumm, B. Wagemann, The oxidation of NiAl, Mater. Corros. 47 (1996) 675–677, https://doi.org/10.1002/maco.19960471203.
[15] M.P. Brady, H. Bei, R.A. Meisner, M.J. Lance, P.F. Tortorelli, Effect of Mo dispersion size and water vapor on oxidation of two-phase directionally solidified NiAl–9Mo in-situ composites, Scr. Mater. 80 (2014) 33–36, https://doi.org/10.1016/j.scriptamat.2014.02.011.
[16] Zs. Wang, Y. Xie, Jt. Guo, Lz. Zhou, Zq. Hu, G.Y. Zhang, Zg. Chen, High temperature oxidation behavior of directionally solidified NiAl–31Cr–2.9Mo–0.1Hf–0.05Ho eutectic alloy, Trans. Nonferrous Met. Soc. 22 (2012) 1582–1587, https://doi.org/10.1016/S1003-6326(11)61359-9.
[17] G. Geramifard, P. Franke, H.J. Seifert, Thermodynamic Modelling of the Ni-Al-Cr-Mo-O System (Unpublished Work), 2020.
[18] J.O. Andersson, T. Helander, L. Höglund, P.F. Shi, B. Sundman, Thermo-Calc and DICTRA, Computational Tools for Materials Science, Calphad, 2002.
[19] M.W. Brumm, H.J. Grabke, The oxidation behaviour of NiAl-I. Phase transformations in the alumina scale during oxidation of NiAl and NiAl-Cr alloys, Corrs. Sci. 33 (1992) 1677–1690, https://doi.org/10.1016/0010-938X(92)90002-K.
[20] D.J. Young, High Temperature Oxidation and Corrosion of Metals, firstst ed., Elsevier, Amsterdam, Boston, London, 2008.
[21] C. Wagner, The evolution of data obtained with diffusion couples of binary single-phase and multiphase systems, Acta Mater. 17 (1969) 99–107.
[22] A. Paul, T. Laurila, V. Vuorinen, S.V. Divinski, Thermodynamics, Diffusion and the Kirkendall Effect in Solids, Springer International Publishing, Cham, 2014.
[23] V.K. Tolpygo, D.R. Clarke, Wrinkling of α-alumina films grown by thermal oxidation—I. Quantitative studies on single crystals of Fe–Cr–Al alloy, Acta Mater. 46 (1998) 5153–5166, https://doi.org/10.1016/S1359-6454(98)00133-5.
[24] J. Peng, X. Fang, Z. Qu, J. Wang, Isothermal oxidation behavior of NiAl and NiAl-(Cr,Mo) eutectic alloys, Corrs. Sci. (2019), https://doi.org/10.1016/j.corsci.2019.02.011.
[25] K.P. Lillerud, P. Kofstad, On high temperature oxidation of chromium, Inorganic-Organic Separators 127 (1980) 2397–2410.
[26] K. Atarashiya, R. Nagasaki, K. Nishida, Interdiffusion in $Al_2O_3$-$Cr_2O_3$ Quasi-binary System, J. Jpn. Inst. Met. 51 (1987) 1018–1022.
[27] B.A. Pint, K.L. More, I.G. Wright, P.F. Tortorelli, Characterization of thermally cycled alumina scales, Mater. High Temp. 17 (2000) 165–171, https://doi.org/10.1179/mht.2000.024.
[28] Hu Lei, Microstructure, Mechanical Properties and Oxidation Resistance of NiAl In-situ Composites, Ph.D Thesis, Aachen, 2005.
[29] P. Saltykov, O. Fabrichnaya, J. Golczewski, F. Aldinger, Thermodynamic modeling of oxidation of Al–Cr–Ni alloys, J. Alloys. Compd. 381 (2004) 99–113, https://doi.org/10.1016/j.jallcom.2004.02.053.